

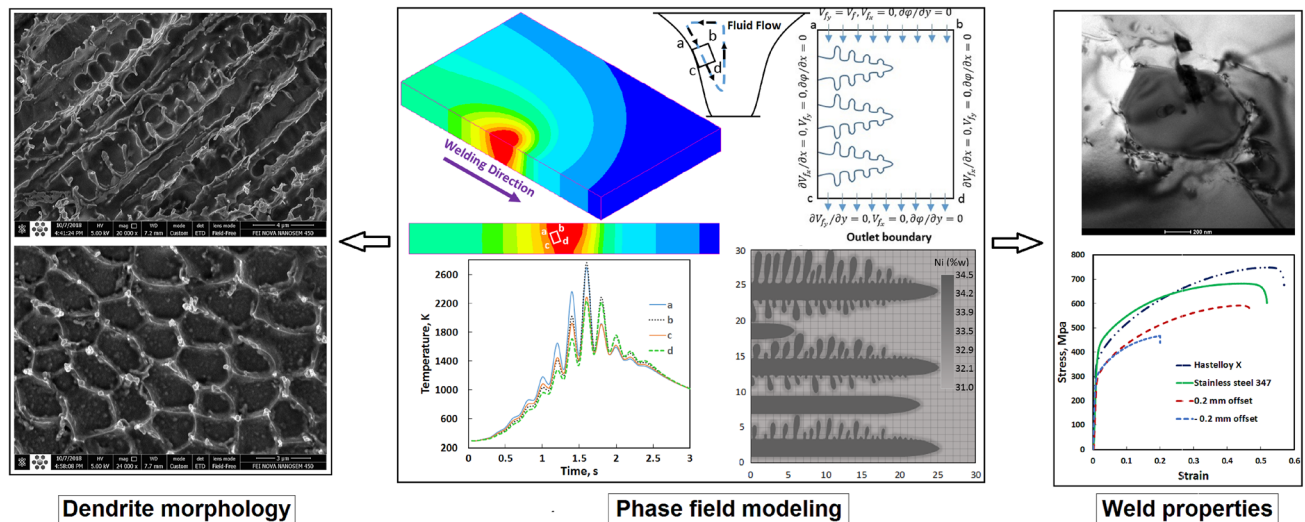
Microstructure and Solidification Cracking Analysis of Dissimilar Pulsed Laser Welded Hastelloy X to 347 Stainless Steel Using Phase-Field Models



TOHID AZIMZADEGAN and SEYED ALI ASGHAR AKBARI MOUSAVI

A phase-field model is utilized to associate the solidification behavior of dendrites to the microscopic characteristics of the weld and to characterize the microstructure evolution in dissimilar pulsed laser welded Hastelloy X to 347 stainless steel alloy. The simulations reveal that the morphology of the dendrites during rapid solidification of the molten zone is affected by a melt flow and dilution level. The effect of melt flow as a result of Marangoni convection is modeled by Boussinesq approximation to adjust the concentration field around a developing dendrite, modifying its growth morphologies. The enhancement of hot cracking resistance is studied by adjusting the microstructure morphology through the possibility of the backfilling of the melt for the most efficient dendrite spacing, which was evaluated by correlation of the heat conduction problem and the phase-field model. Besides, the laser offset was estimated by finding the optimal chemical composition of the weld zone in the ternary Fe-Ni-Cr system that affects the microstructure predicted by the phase-field model. The segregation of nanoparticle compounds analyzed by TEM in interdendritic regions is possible for primary dendrite spacing higher than $3 \mu\text{m}$ and consequently the solidification cracking susceptibility is increased.

Graphic Abstract



<https://doi.org/10.1007/s11663-021-02168-9>

© The Minerals, Metals & Materials Society and ASM International 2021

I. INTRODUCTION

LASER welding is recognized as a progressive process to join materials, where the characteristics of the weld zone are mainly determined by the microstructure evolution that forms while the molten zone is solidifying. The composition of the melted zone and the

TOHID AZIMZADEGAN and SEYED ALI ASGHAR AKBARI MOUSAVI are with the School of Metallurgy and Materials Engineering, College of Engineering, University of Tehran, P.O. Box 11155-4563, Tehran, Iran. Contact e-mail: t.azimzadegan@ut.ac.ir, akbarimusavi@ut.ac.ir

Manuscript submitted October 13, 2020; accepted March 29, 2021.
Article published online May 12, 2021.

welding process conditions themselves have a significant impact on developing microstructures, whose patterns, in turn, affect joint properties.^[1] The laser offset alters the element circulation, grain growth type, phase constitution, and the resulting mechanical properties of weld metal.^[2] On the likelihood, the most engrossing and primarily assessed microstructures in the weld solidification are dendrite morphologies. A consequential occurrence in solidification mechanisms is the columnar to equiaxed transition,^[3] a morphological transformation of the freezing phase microstructure that acts as an important role in the welding process.

The microstructure prediction and particularly the simulation of the dendritic morphology in the weld zone require computationally comprehensive modeling procedures as an example of cellular automata and phase-field models. The effect of process parameters and compositions was investigated by some studies to simulate the morphological progress of the dendrite for various solidification circumstances in the vicinity of the weld pool. Zhan *et al.*^[4] expanded a cellular automata model to predict grain morphologies in the weld pool of Ni-Cr alloy. The phase-field simulation of weld solidification microstructure of Al-3wt pct Cu alloy using different welding speeds investigated by Farzadi *et al.*^[5] Montiel *et al.*^[6] by applying the phase-field method studied the microstructure characterization of magnesium AZ31 alloy under which a columnar to equiaxed transition is maintained under welding conditions. Fallah *et al.*^[7] utilized a quantitative phase-field model that is coupled to a thermal finite element model of the laser powder deposition to predict the solidification morphology of Ti-Nb alloy under the thermal conditions. Taking into account the transient solidification conditions during welding, Zheng *et al.*^[8] elaborated a phase-field model to simulate the dendrite growth near the weld pool boundary. Bailey *et al.*^[9] recently presented a 3D phase-field model to simulate dendrite morphology and microstructure evolution during the laser welding of Al 6061 alloy. Considering the continuously changing solidification parameters in the weld zone, Yu *et al.*^[10] employed a phase-field model to demonstrate the evolution of polycrystalline solidification in the entire weld. Gaoyang *et al.*^[11] utilized the phase-field method to investigate the effect of the dendritic growth contest between dissimilar grains with different crystalline orientations on microstructure development during laser welding of Al-Cu alloy. According to a phase-field model of Geng *et al.*,^[12] the solidification cracking susceptibility during welding is dependent on the difference coalescence behavior between primary and secondary dendrites because of minor solute segregation between primary dendrites and the easier linking of projecting secondary dendrites. Nie *et al.*^[13] also developed a numerical model that unites the finite element method and stochastic model to predict the growth of the microstructure of the IN718 alloy during the laser additive manufacturing process.

Modeling of solidification in the welding process is not concluded lacking considering convection in the molten pool as well. Fluid flow during solidification alters the element distribution fields and the motion of

the interface and might persuade the making of an entirely different growth pattern compared to completely diffusive growth and can modify a characteristic of weld microstructure such as dendrite spacing. The procedure that the melt flux changes the microstructure growth model is the convection of solute fields around the dendrite arm spacing.^[14] Linking the phase-field and diffusion field equations takes into account individual time and spatial grid magnitudes. Jeong *et al.*^[15] studied the influence of fluid flow on the evolution of dendrite utilizing a phase-field computation on a 3D adaptive grid algorithm. They used an averaging technique for the fluid velocity field linked to the phase-field equation. Zhang *et al.*^[16] studied the relevance of forced convection and redistributed solute on the dendritic growth during solidification of the Al-Cu alloys by utilizing the phase-field lattice-Boltzmann method in combination with the adaptive grid refinement algorithm.

In the last two decades, several phase-field models have been developed for the investigation of the dendrite formation during the solidification of binary and multicomponent alloys. Zhao *et al.*^[17] studied the impacts of temperature gradient direction, growth modification, and thermal fluctuation on the microstructure morphologies in the solid-liquid interface of Al-Zn alloy by phase-field model. The microstructure evolution during the rapid solidification of Fe-C and Fe-C-P alloys and the effect of the alloying element on the dendrite morphology at the different temperatures were simulated by Suzuki *et al.*^[18] Kobayashi *et al.*^[19] presented a phase-field model for solidification of Al-Mg-Si alloys, which incorporates the thermodynamic database accompanied by a nonlinear kinetic coefficient. Kim^[20] developed the anti-trapping phase-field model used in multicomponent systems with arbitrary thermodynamic data and derived a correlation of the physical interface mobility and the phase-field mobility at the thin interface limit. Kundin *et al.*^[21] developed an extended multi-component model for the simulation of grain morphologies in a multicomponent Inconel 718 superalloy under the non-isothermal state.

According to the literature review, the phase-field models, in general, have been studied only the microstructure evolution with no insight into the relationships between the processing and properties of the material. In this work, we study the morphology of the columnar and equiaxed dendrite under the limitations in the keeping of those for pulsed laser welding, in which the typical thermal gradients and cooling rates are greater than those of common welding. In laser joints, equiaxed and columnar dendrite morphologies are often the dominant microstructures.^[22] Therefore, the basic purpose of this study is to investigate the effects of dilution level and Marangoni convection on the dendrite morphology in the weld pool and the influence on the primary dendrite spacing from a computational viewpoint by numerical simulations dependent upon the latest advantages in the phase-field modeling. The simulated dendrite morphologies and analogous concentration fields can be utilized as specific items for estimate crack susceptibility. This paper demonstrates the effect of convection on the molten pool in the

Table I. Chemical Compositions of the Hastelloy X and SS 347 Alloys Used in This Study, W Pct

	Ni	Cr	Fe	Mo	Co	W	C	Mn	Si	B	Nb
Hastelloy X	bal	22.1	17.0	8.8	1.7	0.9	0.058	0.4	0.35	0.002	—
SS 347	10.8	18.0	bal	0.4	0.1	—	0.045	1.6	0.52	0.002	0.653

Table II. Laser Process Parameters of Dissimilar Joining of SS-347 to Hastelloy X

Frequency (1/s)	Pulse Duration (ms)	Welding Speed (mm/s)	Pulse Energy (J)	Heat Input (J/mm)	Laser Offset (mm)
6	7	3.5	5.5	9.4	[− 0.2, 0.2]

conditions of directional solidification. Moreover, the mechanism that causes the changes in the dendrites spacing under the influence of convection is completely clarified.

II. EXPERIMENTAL PROCEDURES

The materials utilized were Hastelloy X and stainless steel 347 sheets with a thickness of 1mm. Their chemical compositions are shown in Table I.

The workpiece preparations were performed previous to welding. The plate sides are polished to eliminate the surface oxide, continued with the cleaning by acetone to impede weld metal contamination. The laser origin was a pulsed Nd:YAG micro laser apparatus, which creating square pulses with a peak mean power of 80 W. Weld pool protection carried out using a side nozzle argon gas with a 3 L/min flow rate. The workpiece joint method was butt welding. The laser process parameters are disclosed in Table II. The parameters were adopted in compliance with the preliminary examinations in such a way as to acquire joints with appropriate varieties of shape, which are penetration and width and a low level of spatter. The welded joints were assembled with different laser offsets from 0.2 mm to stainless steel 347 alloy to 0.2 mm to Hastelloy X alloy and with a distance of 0.1 mm.

The dendrite morphologies and weld microstructure were examined using scanning electron microscopy in the secondary electron mode. Besides, to determine the precipitation compositional elements, EDS analysis was performed. The weld pieces were subdivided normal to the welding direction and afterward, the metallography samples were made by grinding and polishing on the disc and eventually electrolytically etched in a solution of 65 mL HNO₃ + 35 mL H₂O using a platinum cathode at 6 V.

Interdendritic fine compound identification was completed using an FEI Tecnai G² F20 transmission electron microscope (TEM, 200 kV accelerating voltage) to acquire SAD patterns at a superior symmetry zone axis. The TEM specimens with a 3 mm diameter disc configuration were made by grinding the disc to ~ 80 μm and subsequently twin jet polished in 100 mL Perchloric acid + 900 mL Methanol at − 25 °C and 20 V.

Mechanical tests are principally utilized to prove that the weld metal is not the defective joint in the optimum range of welding parameters. Transverse tensile tests were carried out according to the ASTM E 8 standard.

III. PHASE FILED MODEL

A thermodynamically consistent phase-field model in consideration of rapid solidification of a multi-component system is utilized to model the morphology of microstructure in the weld zone in the pulsed laser welding of Hastelloy X to 347 stainless steel. To save computation time and for simplification, we consider the equivalent composition of Cr and Ni, *i.e.*, Cr_{eq} and Ni_{eq}, and Fe as system components.

In attendance, the phase-field model is established upon the theories expanded in the thermodynamically consistent procedure of Kim,^[20] Kundin *et al.*^[21] on the subject of multicomponent alloys, and based on the approach of Siquieri *et al.*^[23] for the fluid flow. The phase-field equation during the solid phase transformation is defined as

$$\begin{aligned} \tau a_s(\mathbf{n})^2 \frac{\partial \varphi_i}{\partial t} = & \nabla \cdot [W^2 a_s(\mathbf{n})^2 \nabla \varphi_i] \\ & + \partial_x \left(|\nabla \varphi|^2 W a_s(\mathbf{n}) \frac{\partial W a_s(\mathbf{n})}{\partial (\partial_x \varphi)} \right) \\ & + \partial_y \left(|\nabla \varphi|^2 W a_s(\mathbf{n}) \frac{\partial W a_s(\mathbf{n})}{\partial (\partial_y \varphi)} \right) \\ & - 2\varphi_i(1 - \varphi_i)(1 - 2\varphi_i) + \varphi_i^2(1 - \varphi_i)^2 \frac{a_1 W}{\sigma} \Delta G_{ij} + \xi_i \end{aligned} \quad [1]$$

where τ is the kinetic coefficient, W is the width of the interface, a_1 is a numeric constant, σ is the interface energy and $a_s(\mathbf{n}) = 1 + \epsilon_4 \cos(4\mathbf{n})$ is a fourfold anisotropic function that gives reasons for anisotropic surface energy and kinetics. ΔG_{ij} is the chemical driving force of the evolution of phase i in a phase j that for a multicomponent alloy, can be defined as

$$\Delta G_{ij} = \sum_A \Delta A_{ij}^A X_i^A \frac{(c^A - c^{A,eq})}{h_i^A(\bar{\varphi})} \quad [2]$$

where $\Delta A_{ij}^A = A_i^A - A_j^A$ is the equilibrium concentrations difference of liquid and solid phases, $h_i^A(\bar{\varphi}) = (\varphi + (1 - \varphi)k_i^A)$ is the partition coefficient function matrix, X_i^A is the liquid phase thermodynamic factor and k_i^A is the partition coefficient.

The Gaussian noise distribution is appended to Eq. [1] so that generates unsystematic instabilities at the interface. It can be explained as

$$\xi = \xi_0 r \varphi_i^2 (1 - \varphi_i)^2 \quad [3]$$

where ξ_0 is a magnitude of the noise and $r \in [-1; 1]$ is a random value. The continuity problem in the terms of the phase mobilities and the alloy concentration in the case of rapid solidification in pulsed laser welding can be given by

$$\begin{aligned} \frac{\partial c^A}{\partial t} = \nabla \cdot \sum_B \left(\sum_j D_j^{AB} k_{ij}^B q_i \right) \nabla \left(\frac{c^B - c^{B,\text{eq}}}{h_i^B(\bar{\varphi})} \right) - \nabla \cdot \mathbf{J}_{\text{at}}^A \\ - \sum_B (1 - \varphi) (\mathbf{V}_f \cdot \nabla) \left(\frac{c^B - c^{B,\text{eq}}}{h_i^B(\bar{\varphi})} \right) \end{aligned} \quad [4]$$

where the last term in the right-hand side of the continuity equation is accountable for the convection in the weld pool. $q_i = (1 - \varphi) + (1 + \varphi) \frac{D_i}{D_j}$ is the model function, V_f is the fluid velocity and \mathbf{J}_{at}^A is the anti-trapping current, which gives rise to a net solute motion from solid to liquid phase in the normal direction \mathbf{n} to the interface which counteracts the solute trapping and gives back chemical equilibrium at the interface. The anti-trapping current subject to the thin-interface problem has the following form

$$\mathbf{J}_{\text{at}}^A = 2a_{\text{at}} W \left(1 + \left(1 - k_{ij}^A \right) \frac{(c^A - c^{A,\text{eq}})}{\Delta A_{ij}^A} \right) \Delta A_{ij}^A \frac{\partial \varphi_i}{\partial t} \mathbf{n}_{ij} \quad [5]$$

where $\mathbf{n}_{ij} = \frac{\nabla \varphi}{|\nabla \varphi|}$ is the normal vector toward the i/j interface and $a_{\text{at}} = 1/2\sqrt{2}$.

The kinetic parameter τ in Eq. [1] can be taken from the continuity interface constraint as

$$\tau = \frac{a_1 a_2 W^3}{\sigma} \sum_B Q_L^A \quad [6]$$

where Q_L^A is the growth limitation factor of alloy components explained as

$$Q_L^A = \frac{\bar{X}^A |\Delta A_{ij}^A|^2}{D_L^A} \quad [7]$$

where \bar{X}^A is the mean thermodynamic factor. It should be noted that this equation is justified for the weld metal with an ordinary convection flow that is compatible with a small Peclet number $P_e = V_\infty R_{\text{tip}} / 2D \ll 1$. Here V_∞ is a rate of the fluid flow, R_{tip} is a dendritic tip mean radius.

Note that to simulate the development of dendrite morphology during rapid solidification, a heat conduction problem has to be explained concurrently with the phase-field and continuity equations. The parameters $c_i^{A,\text{eq}}$, ΔA_{ij}^A and τ adjust with temperature and must be computed in each computational step as

$$c_i^{A,\text{eq}} = c_i^{A,\text{eq}}(T_0) + \frac{(T - T_0)}{m_{i,\varphi}^A} \quad [8]$$

$$\Delta A_{ij}^A(T) = \Delta A_{ij}^A(T_0) + \frac{(T - T_0)}{m_{L,\varphi}^A} (1 - k_s) \quad [9]$$

To our model, we add Marangoni convection with varying values as specified by Boussinesq approximation. The Boussinesq estimation is utilized to justify the density variation on account of the temperature changes. The modified Navier–Stokes equations are utilized to compute the velocity of flow V_f . The Navier–Stokes equations are expressed as^[24]

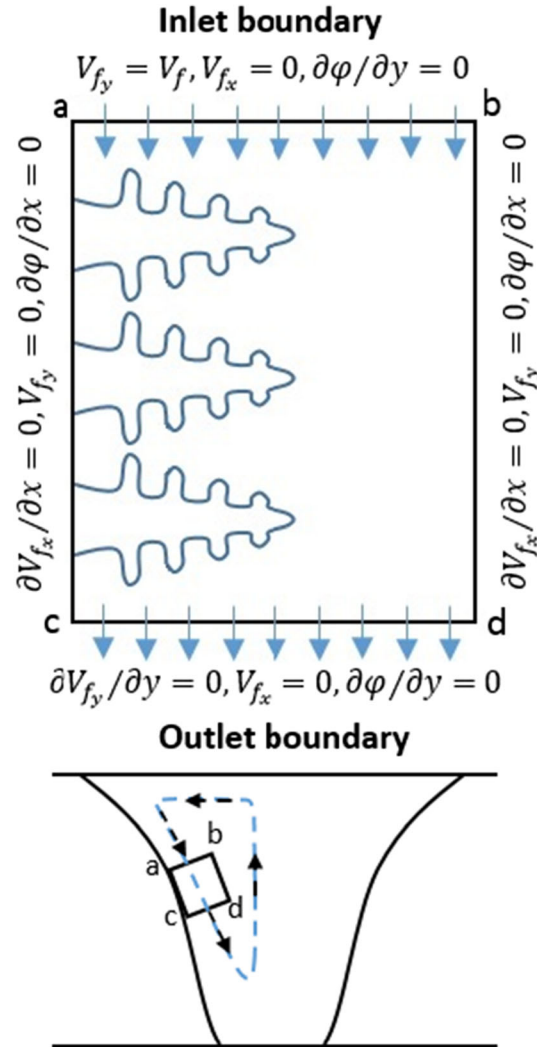


Fig. 1—Computational area and boundary conditions are used to model the microstructure evolution in the weld pool.

$$\frac{\partial(1-\phi)V_f}{\partial t} = -(1-\phi)(V_f \cdot \nabla)V_f - (1-\phi)\nabla \frac{p}{\rho_0} + \nabla[\mu\nabla(1-\phi)V_f] - 2h\mu \frac{\phi^2(1-\phi)}{W^2} V_f \quad [10]$$

where p is the pressure, μ is the kinematic viscosity and ρ_0 is the density of the liquid phase. The last term in Eq. [10], with a constant h , is the dispersive interfacial force per unit volume. The continuity equation takes the following form

$$\nabla[(1-\phi)V_f] = 0 \quad [11]$$

Negative $d\gamma/dT$ when surface active element concentration is low; This would lead to the surface temperature being higher than the critical temperature, thus the surface tension is lower in the high-temperature region, the pool center; therefore according to Marangoni convection theories, liquid metal would experience an outward flow from the pool center. Since surface tension coefficients and thermal gradients are negative, the surface melt flows caused by Marangoni convection on both sides are outward.

IV. NUMERICAL APPROACH

Figure 1 illustrates the calculative area and boundary conditions applied to model the microstructure evolution in a laser welding process. The simulation domain is $100 W \times 150 W$. Assuming complete mixing of the two alloys in the weld zone for all modes of laser offset, the simulation location in the weld pool was selected in a position in which columnar dendrites were stable at a certain temperature gradient and cooling rate. The phase-field equations are discretized employing a finite difference method. Note that, for the high order term the second-order discretization and for the time the first-order discretization is utilized. The grid spacing utilized in the finite difference method was equal to $\Delta x/W = 0.5$. As seen in Figure 1, absolutely not flux boundary conditions are implemented in the right and left boundary in addition to periodic boundary conditions on the bottom and topsides. An Euler explicit approach is applied to solving the phase-field equations. The

Table IV. Computational Phase-Field Model Parameters

Computational Property	
Kinetic Coefficient, τ , ((mm/s K))	1.95
Width of the Interface, W (mm)	0.002
Anisotropy Coefficient, ϵ_4	0.01
Numeric Constant, a_1	0.47
Amplitude of the Noise, ξ_0	0.4
Fluid Velocity, V_f (m/s)	0.05 to 0.3
Anti-Trapping Coefficient, a_{at}	$1/2\sqrt{2}$
Δt	2×10^{-3}
$\Delta x, \Delta y$, ((μm))	1
Pressure, P (kPa)	101.325

modified Navier-Stokes equations are solved using the Semi-Implicit Method for Pressure Linked Equations Revised method.

At the liquid/solid interface in the weld pool, the fluid flow direction is approximately tangent to the molten boundary. Consequently, the liquid metal flow velocity direction applied to simulate the microstructure growth in the molten zone is supposed to be perpendicular to the liquid/solid interface normal. In order to evaluate the effects of various inlet melt velocity on the dendritic growth, simulations were carried out at different inlet fluid velocity in the range of 0.05 to 0.3 mm/s. Indeed, the magnitude of the initial fluid velocity is concluded to be uniform during the simulation. For melt flow the top and bottom sides were assumed to be at constant velocity. A symmetrical boundary condition has been assumed for the top and bottom sides, wherein the velocity gradient parallel to the boundary and the velocity perpendicular to the boundaries are set to zero. The simulation was carried out utilizing relevant computational and material parameters as taken in Tables III and IV. The material properties of the different alloys are acquired by the materials modeling database JMatPro.

The thermal equation applied in the phase-field model to predict microstructure evolution in the laser welding process is defined as

$$T(z, t) = T_0 - \frac{dT}{dt}t + G(t) \left(z - \int_0^t V_z(t)dt \right) \quad [12]$$

Table III. Material Parameters for the Model Alloys

Material Property	Ni40-Fe32-Cr28	Fe43-Ni31-Cr26	Fe37-Ni36-Cr27
Surface Tension (N/m)	1.860	1.851	1.845
Surface Tension Temperature Coefficient (N/m K) 10^4	- 3.36	- 3.30	- 3.28
Liquidus Temperature (K)	1398	1410	1405
Solidus Temperature (K)	1355	1360	1357
Heat of Fusion (kJ/kg)	219	204	212
Specific Heat of Solid (J/kg K)	440	430	440
Specific Heat of Liquid (J/kg K)	710	700	710
Dynamic Viscosity (kg/m s)	7.8×10^{-3}	7.89×10^{-3}	7.84×10^{-3}
Thermal Conductivity of Liquid (W/m k)	29.26	32.40	32.49
Density of Liquid (kg/m 3)	7310	7400	7420

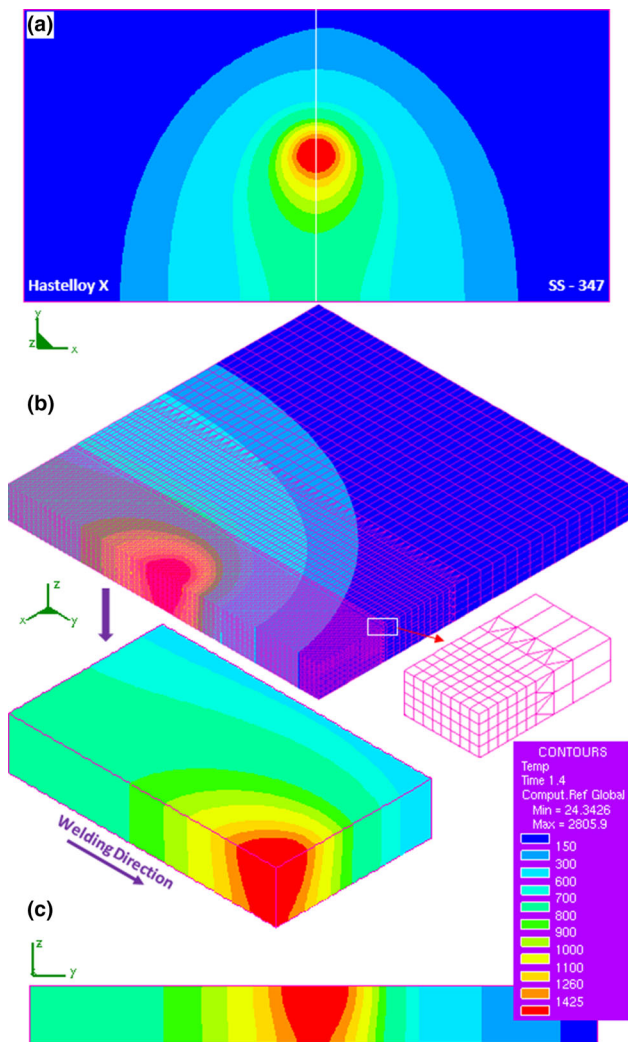


Fig. 2—Predicted temperature distribution at the welding speed of 3.5 mm/s, (a) unsymmetrical temperature field of the dissimilar pulsed laser welded Hastelloy X to 347 stainless steel, (b) the 3D finite element thermal model of laser welding, (c) the temperature field of longitudinal section at the weld centerline.

where T is the thermal field that be acquired from the simulation data of thermal process, $T_0 = T(0, t)$ is a reference temperature, z is the axis in the direction of the dendrite progression direction. V_z is the pulling velocity of the solid/liquid interface and G is the temperature gradient at the weld pool boundary. The reference temperature T_0 , which is merely the initial temperature of the left boundary, was fixed on the solidus temperature. In addition, the effect of fluid flow on microstructure evolution during welding is taken into account. The cooling rate and temperature gradients for the pulsed laser welding are estimated applying the transient heat transfer SYSWELD model as described in Reference 22. The predicted temperature distribution on the top view and longitudinal section at the weld centerline are shown in Figure 2. Unsymmetrical temperature field of the dissimilar pulsed laser welded Hastelloy X to 347 stainless steel

is discernible in Figure 1(a). Owing to computational indispensability, the phase-field calculative area is considerably smaller than the pulsed laser welding model's computational domain. The phase-field model's domain size is $200 \mu\text{m} \times 300 \mu\text{m}$ while the welding model simulation's domain is much larger, with the dimensions $10 \text{ mm} \times 10 \text{ mm} \times 1 \text{ mm}$ for each of the alloys, as shown in Figure 2. Throughout the phase-field models at each time step, due to the different mesh sizes between the macro scale model and phase-field simulations, temperature history are interpolated from the welding model data onto the phase-field mesh.

The simulation results of the welding thermal process are shown in Figures 2 through 4. Typically, the temperature gradients were derived in the weld pool along Line 1 (depth of the weld zone) and Line 2 (width of the weld zone), as seen in Figure 3(a). The temperature data decline nonlinearly from the center to the fusion line of the weld pool. Particularly, the temperature gradient in the weld pool is lower than the rate weld pool/base metal interface, and the thermal gradient along the depth of the weld zone is lower than the gradient along width.

The cooling rate of temperature field is determined based on the temperature between solidus and liquidus, as shown in Figure 2(b). Only the solidification temperature range was selected for the phase-field simulations. Base on the macro scale model, the cooling rates inside the phase-field model are almost 14,000 K/s between liquidus and solidus temperatures. The temperature distribution of longitudinal section at the weld centerline with advancement of pulsed laser beam is shown in Figure 4(a). As time advances, the temperatures in the phase-field domain decrease. The temperature curves of four points a, b, c, and d from Figure 4(a) were traced out during the welding model as shown in Figure 4(b).

Using computational modeling, we scrutinize how the variation of system composition affects the dendrite morphology for a specified solidification condition. Especially, all of the initial and boundary conditions, that is, the undercooling, thermal gradient, were fixed and just, as it chose a ternary Fe-Ni_{eq}-Cr_{eq} system for this model.

For modeling the microstructure evolution during laser welding, some assumptions are demonstrated:

1. For laser welding without any laser offset, it was supposed that the same volume of Hastelloy X and 347 were melted. Note that the thermal conductivity of both alloys is almost the same at their melting point.
2. A set of phase-field equations was carried out for various alloy compositions of Fe₄₃-Ni₃₁-Cr₂₆, Fe₃₇-Ni₃₆-Cr₂₇, and Ni₄₀-Fe₃₂-Cr₂₈ according to 0, 0.1, and 0.2 mm offset to Hastelloy X, respectively.
3. The preliminary undercooling was contrived at 20 K calculated from the equilibrium liquidus line of the phase diagram at a particular composition of the alloy.

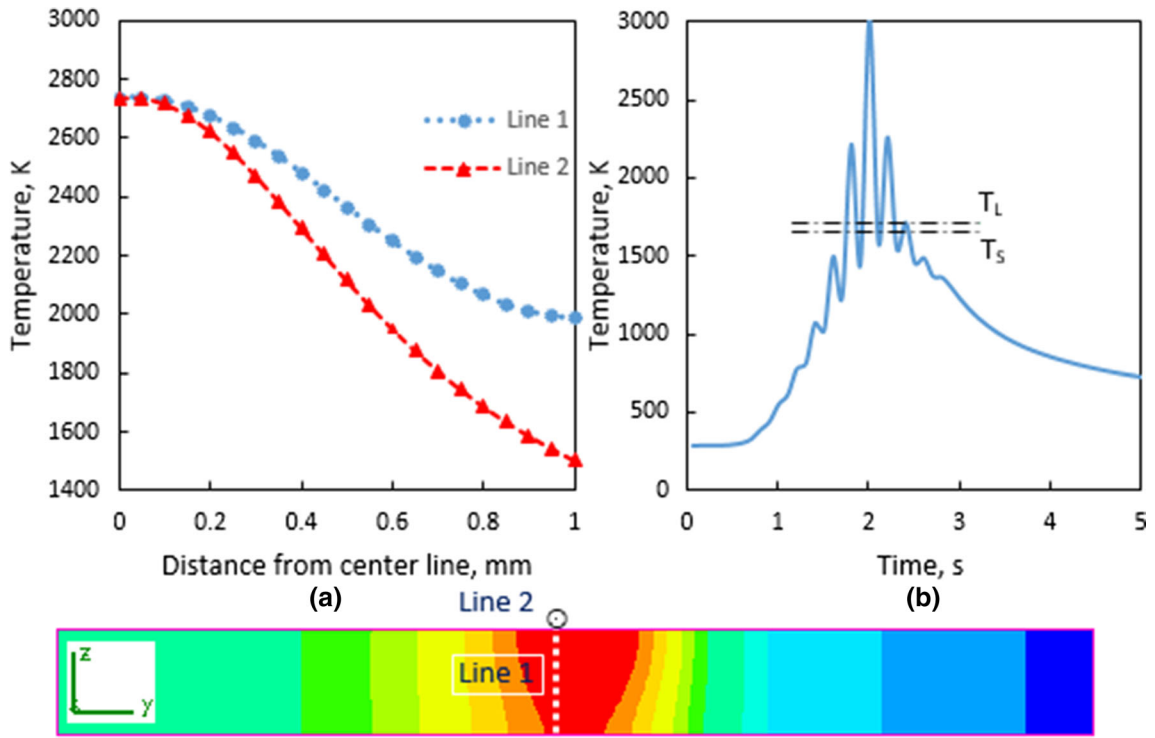


Fig. 3—(a) Temperature gradient in the weld pool along Line 1 (depth of the weld zone) and Line 2 (width of the weld zone), (b) predicted time-temperature profile in the center line at point of $y = 7$ mm.

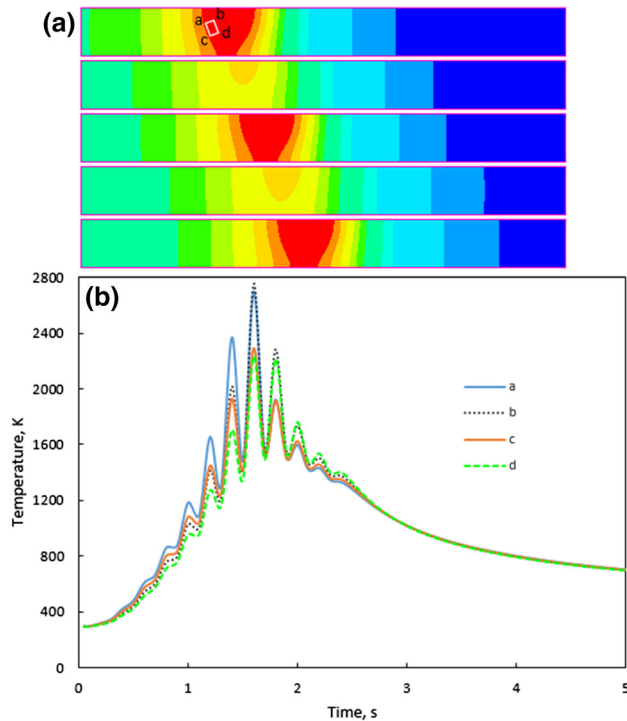


Fig. 4—(a) The temperature fields of longitudinal section at the weld centerline, as time advances (The indicated portion represents the phase-field domain), (b) Temperature profiles of points a, b, c, and d.

V. RESULTS AND DISCUSSION

A. Characterization of the Morphology of the Dendrites in the Weld Zone

Two kinds of microstructure *i.e.*, columnar dendritic and cellular dendritic were perceived in the molten zone, as seen in Figure 5. The distinctive morphological evolution in the weld pool was ascribed to the circumscribed cooling effects and melt composition during solidification.

As seen in Figures 6 and 7, the morphology of the columnar and equiaxed dendrites inside the molten zone have been considered by microscopic analysis, and hence the phase-field model can be applied to associate the solidification behavior of dendrites to the microscopic characteristics of the weld metal. Moreover, the validation of the phase-field model in terms of the primary and secondary dendrite arm spacing can be conceived in Figure 7. All primary dendrites, as shown in Figure 7 progress with almost identical velocities from the initial constituent. The average primary dendrite spacing obtained by experiments is about 3 to 4 μm which is a little larger than that of 3 μm acquired by the simulation result. While secondary dendrites unequally originate from each primary dendrites to the upper and lower sides, showing different spacing in relation to the convection side of the melt flow. As seen in Figure 6, the downward secondary dendrite growth will be totally developed if the convection had lower magnitudes,

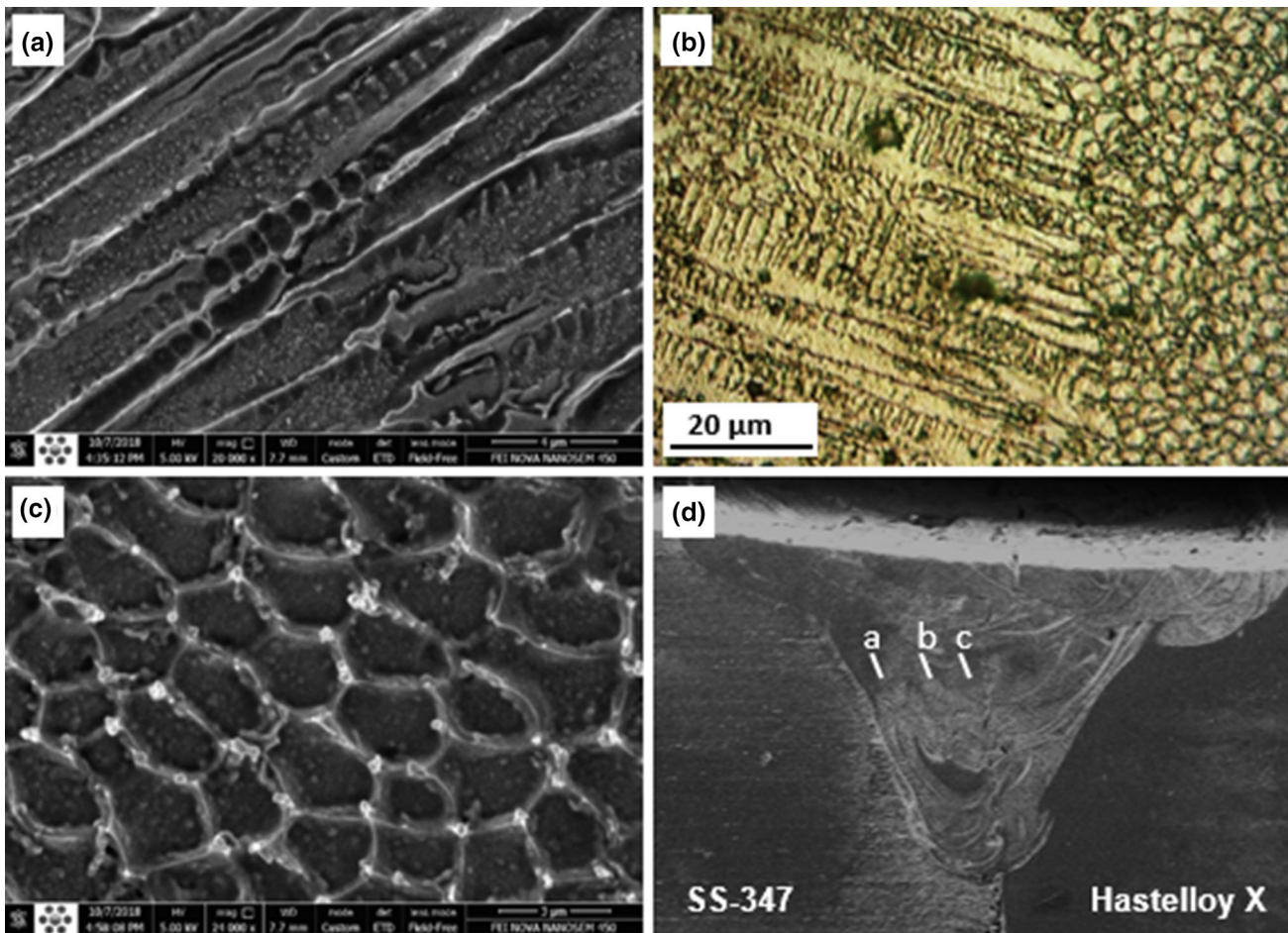


Fig. 5—Solidification structure of the pulsed laser welded Hastelloy X to 347 stainless steel: (a) columnar dendritic solidification (b) transition from columnar to equiaxed dendrites (c) equiaxed dendritic solidification (d) weld zone.

indicating the competitive relationship between convection and undercooling in controlling the dendritic evolution. So, for the initial fluid velocity of 0.05 m/s, anisotropy can be further adjusted by changing the undercooling. Also, as seen in Figure 6(b), for spot laser welding by lower convection, equiaxed dendrites morphology in center of weld pool validated completely phase-field model. The competition of temperature gradient and constitutive undercooling on the solid/liquid interface results in the acute-angled between primary and secondary dendrites. The thermal gradient orientation, indeed, primary dendrite advance direction, is the orientation of lowest energy, acquired as the consequence of anisotropic surface energy and heat flow direction. The comparison between the dendrite morphology in phase-field model with that in experiment, depicts that in both of them there is the phenomenon that secondary dendrite progresses at an angle with a velocity constituent perpendicular to the primary dendrite orientation.

TEM analysis was performed to perceive the nanoparticle structure in the weld zone during the laser welding process. It is properly affirmed by TEM and SEM/EDS analysis that revealed the appearance of Mo,

Nb abundant phases segregated at the dendritic arms (Figures 8 and 9). Figure 8 discloses TEM bright-field micrographs and corresponding SAD patterns taken at the dendrite zone at the laser offset of + 0.1 mm.

Two different precipitation morphologies were evident from the bright filed micrograph as shown in Figure 8. Based on the SAD pattern calibration results in Figures 8(b) and (d) the precipitation phases at the weld pool were indexed as M_6C . As shown in Figure 8(e) the M_6C phase was rich in Mo, besides also containing significant amounts of Cr, Ni, and Fe. This could be elucidated as Mo and Nb have caused segregation during the final solidification. The segregated compounds can bring about the amount of low-melting phases and crack sensitivity. Figure 10 demonstrate SEM of characteristic weld cracks which clearly show solidification structures on the crack surface indicating a weak interdendritic circumstance using the arrow in Figure 10(b). In this area, the Nb content was as high as 68 pct and NbC compounds formed. The formation of such cracks may be ascribed to the complex stress distribution in the weld zone during solidification as described in previous work.^[22]

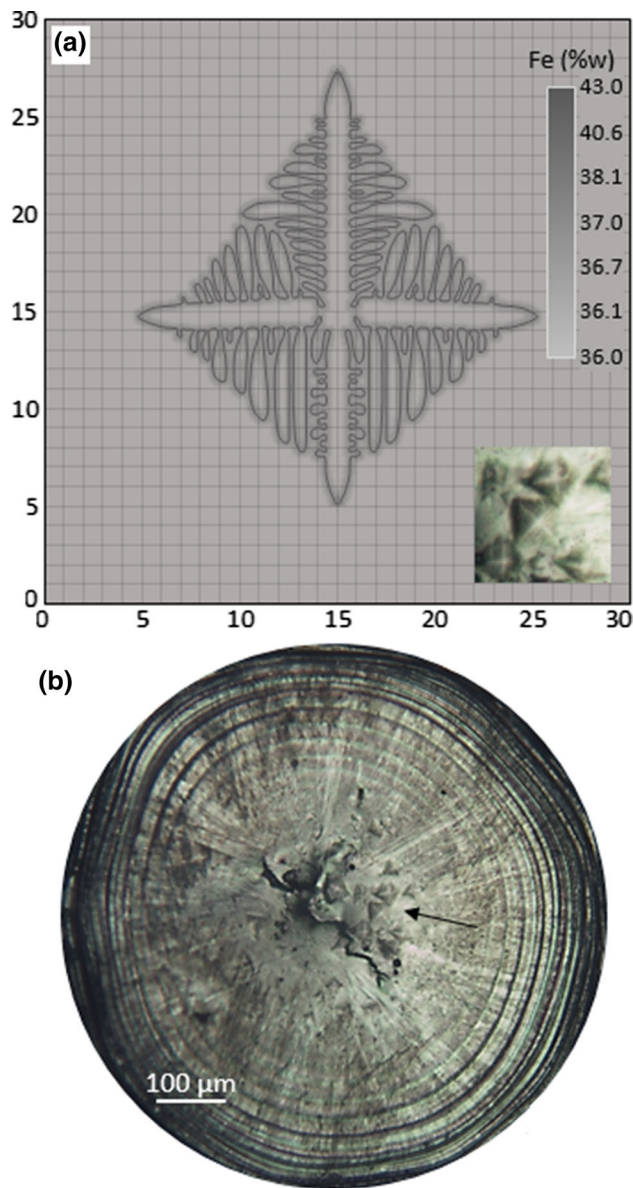


Fig. 6—Morphology of the equiaxed dendrites of the pulsed laser welded Hastelloy X to 347 stainless steel: (a) predicted by phase field model for the initial fluid velocity of 0.05 m/s, (b) equiaxed dendrites formed inside the weld zone in the top view of the spot weld.

In general, the Mo and Nb carbides revealed in the weld pool are conducive to the origin of the solidification crack by reacting with the encircling matrix to emerge a low melting component that easily permeates the grain boundaries of the weld zone.

B. Offset Level of the Laser Beam

Experimental results reveal that principal cracks in the weld pool transpire in incompetent misalignment and that a perfect weld will be unfeasible to generate if the misalignment is greater than 0.3 mm, as shown in Figure 11.

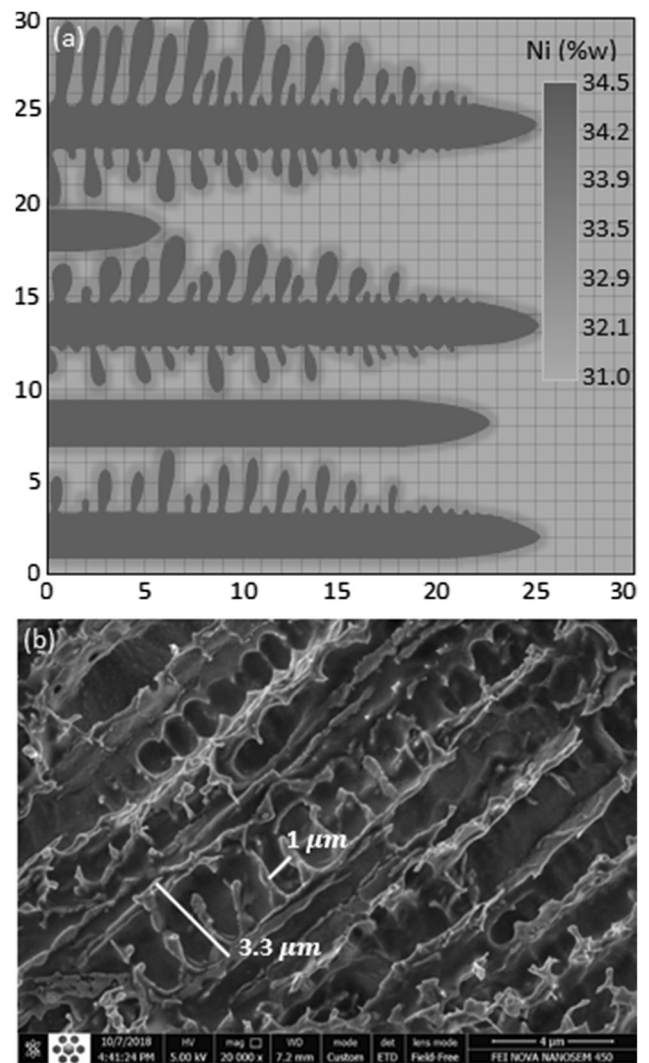


Fig. 7—Morphology of the columnar dendrites of the pulsed laser welded Hastelloy X to 347 stainless steel without the laser offset: (a) columnar dendrites predicted by the phase field model (b) scanning electron micrograph of columnar dendrites.

Admissible joints can be produced by pulsed laser welding accompanied by misalignments practically in the range 0.2 to 0.3 mm towards the Hastelloy X.

Dilution is explained as a percentage contribution of stainless steel 347 to the weld pool, can be defined as:

$$D = \frac{C_{wp} - C_H}{C_{347} - C_H} \quad [13]$$

where C_{wp} , C_{347} and C_H are the element compositions in the weld pool, 347 and Hastelloy X respectively. To adjust the dilution rate of the system elements in the weld pool, the phase-field model was conducted with the differing composition of Ni, Cr, and Fe elements to design misalignments of the laser beam towards the Hastelloy X and 347.

Figure 12(a) shows that the predicted average columnar dendritic spacing of weld increases when the laser beam offset inclines to 347 stainless steel. For the predicted dendrite morphologies (see Figures 6 and 7),

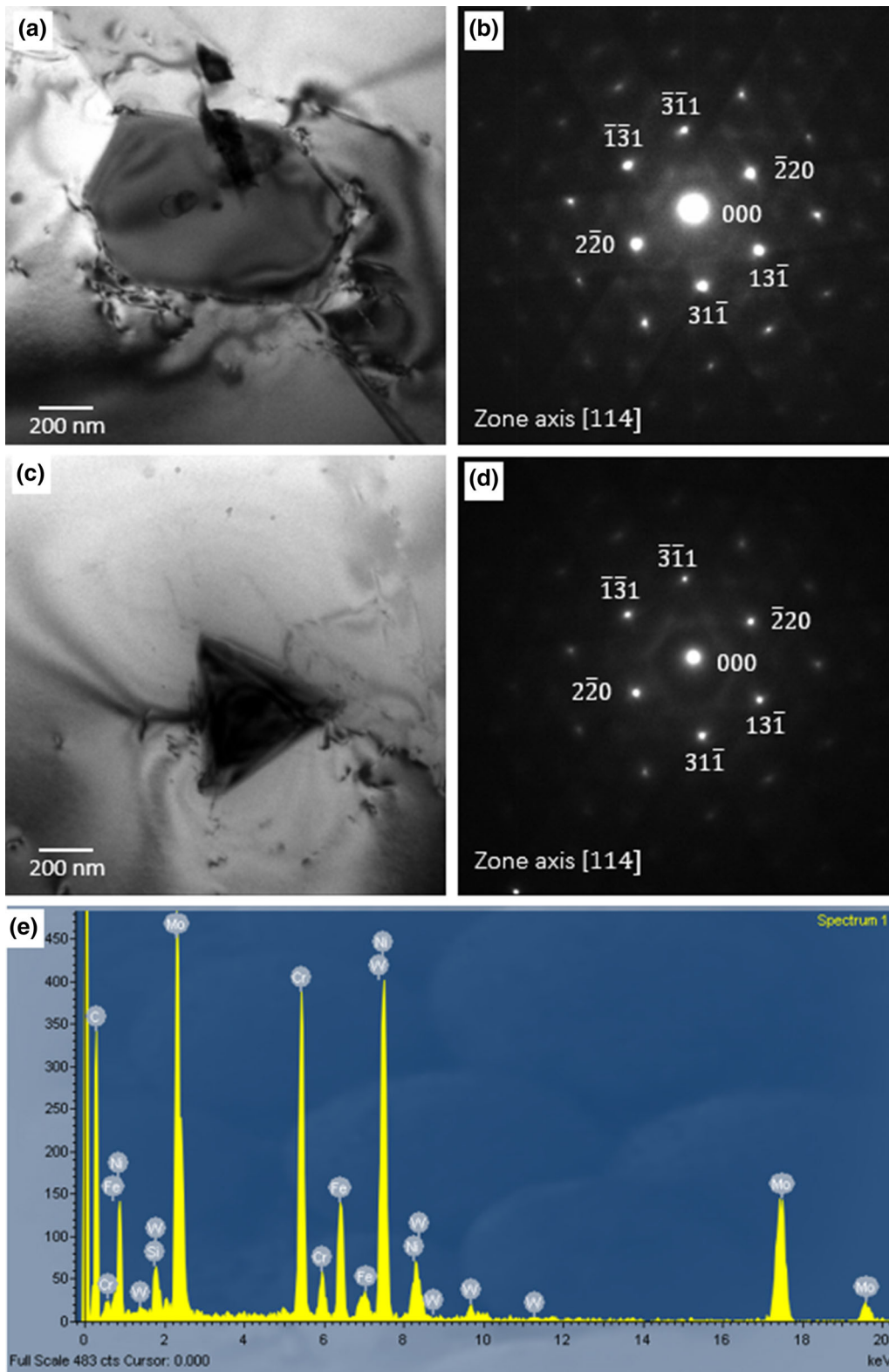


Fig. 8—Transition electron micrographs of Mo-compound in weld zone: (a) at the boundary of the equiaxed dendrite, (b) [114] zone SADP of M_6C , (c) inside of equiaxed dendrite, (d) [114] zone SADP of M_6C , (e) EDS spectra of M_6C .

the main dendrite arm spacing was approximated by including the number of arms using a cut through the line approach in the simulation area. The computational

zone width was afterward apportioned by the number of arms enumerated to acquire the mean dendrite arm spacing. The average columnar spacing changes from

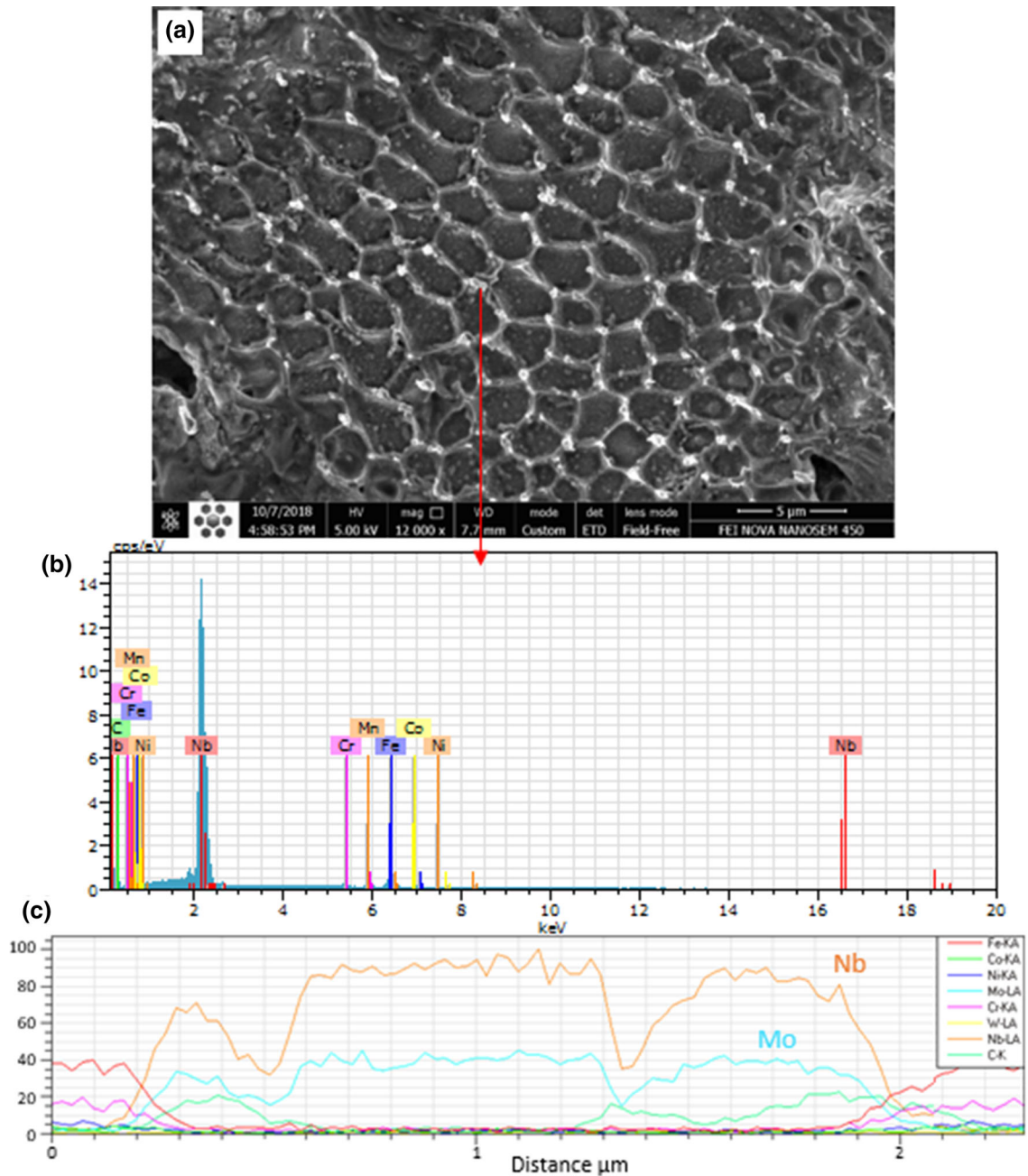


Fig. 9—Scanning electron micrographs of Nb-compound in weld zone: (a) at the boundary of the equiaxed dendrite, (b) EDS spectrum, (c) EDS line spectrum.

0.7 to 2.5 μm . From the above results, it is found that the laser beam offset is more critical in microstructure evolution that affords a fine grain morphology and a minimum spacing between primary dendrites for a 0.2 mm beam offset. Figure 12(b) depicts the evolution of secondary dendrites during solidification as the dendrite tip progresses. As can be comprehended employing the phase-field model, bulky secondary dendrite arms enlarge due to the disbursement of tiny ones by way of solidification advances. Inasmuch larger dendrite arms own less surface area per unit volume, the entire surface energy of the weld joint could be lessened if bulky dendrite arms become larger due to the expense of the

small dendrite arms. It can be found that the secondary dendrite arm spacing decreases with highly spreading the equivalent concentration of Ni and Cr by decreasing dilution. The wider the solidification temperature range, the prolonged time accessible for coarsening, and the higher the secondary dendrite arm spacing.

The effect of dilution level on the morphology of dendrites, which is illustrated in Figure 11, was explicitly correlated with the solidification temperature range and the quantity and dispersion of carbide compounds appeared on the solidified grain boundaries. As dilution was reduced, the Nb compounds decreased and the number of segregated phases reduced. Furthermore, the

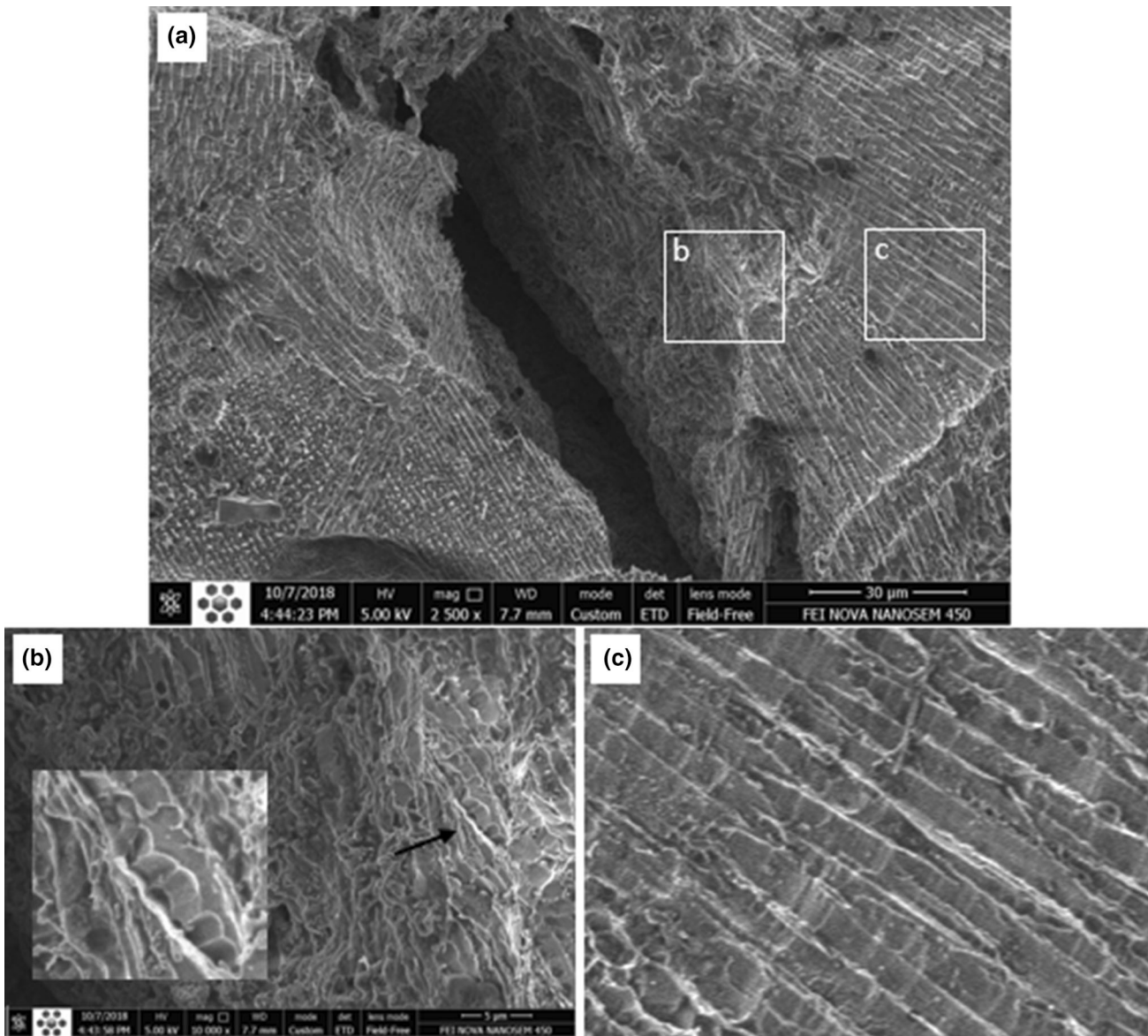


Fig. 10—(a) SEM micrograph of the characteristic crack surfaces of the weld a weak interdendritic segregated compound, (b) the magnification of a the weak interdendritic segregated compound, (c) the dendrite structure in the vicinity of the crack domain.

solidification temperature range increased on multiplying dilution in every offset, so that for alloy compositions of $\text{Fe}_{43}\text{-Ni}_{31}\text{-Cr}_{26}$, $\text{Fe}_{37}\text{-Ni}_{36}\text{-Cr}_{27}$, and $\text{Ni}_{40}\text{-Fe}_{32}\text{-Cr}_{28}$ it was simulated at 14 °C, 10 °C and 7 °C respectively. Infinitesimal modifications in Fe, Ni, and Cr affect the final solidification temperature, logically concurrent with the solidification principle, in that discloses which the growth process preference is controlled as a result of the change of the alloy composition. The predicted composition encompassed in the core of the dendrites and at the inter-dendritic area is illustrated in Figure 13(a). The phase field simulation was validated extensively through comparisons with the EDS analysis of the solutes concentration in the dendrite zones. As illustrated in Figures 13(c) and (d), alloy composition in the core of the dendrites and at the interdendritic area were in good agreement with the

predicted composition. As shown in Figure 7, partly close areas are surrounded by primary and secondary dendrite arms. Fe solutes pile up at the enclosed areas since the diffusion of Fe solutes suppresses between these encompassed zones and its adjacent molten zones.

It is pointed out that the concentration of Fe solutes in the dendrite core is lower than the concentration in the amassed areas surrounded by the dendrite arms. Also, the Fe concentration in the primary concentration is lower than the last melt. Since the growth is accelerating, hence, there is not so much time for the diffusion of Fe in the final solidification, consequently inducing an addition to the concentration in the interdendritic melt. It has been observed that the augmentation of Fe in the weld melt takes place by multiplying dilution, increasing the segregation feasibility of Mo and Nb.^[25] It must be noted that the predicted

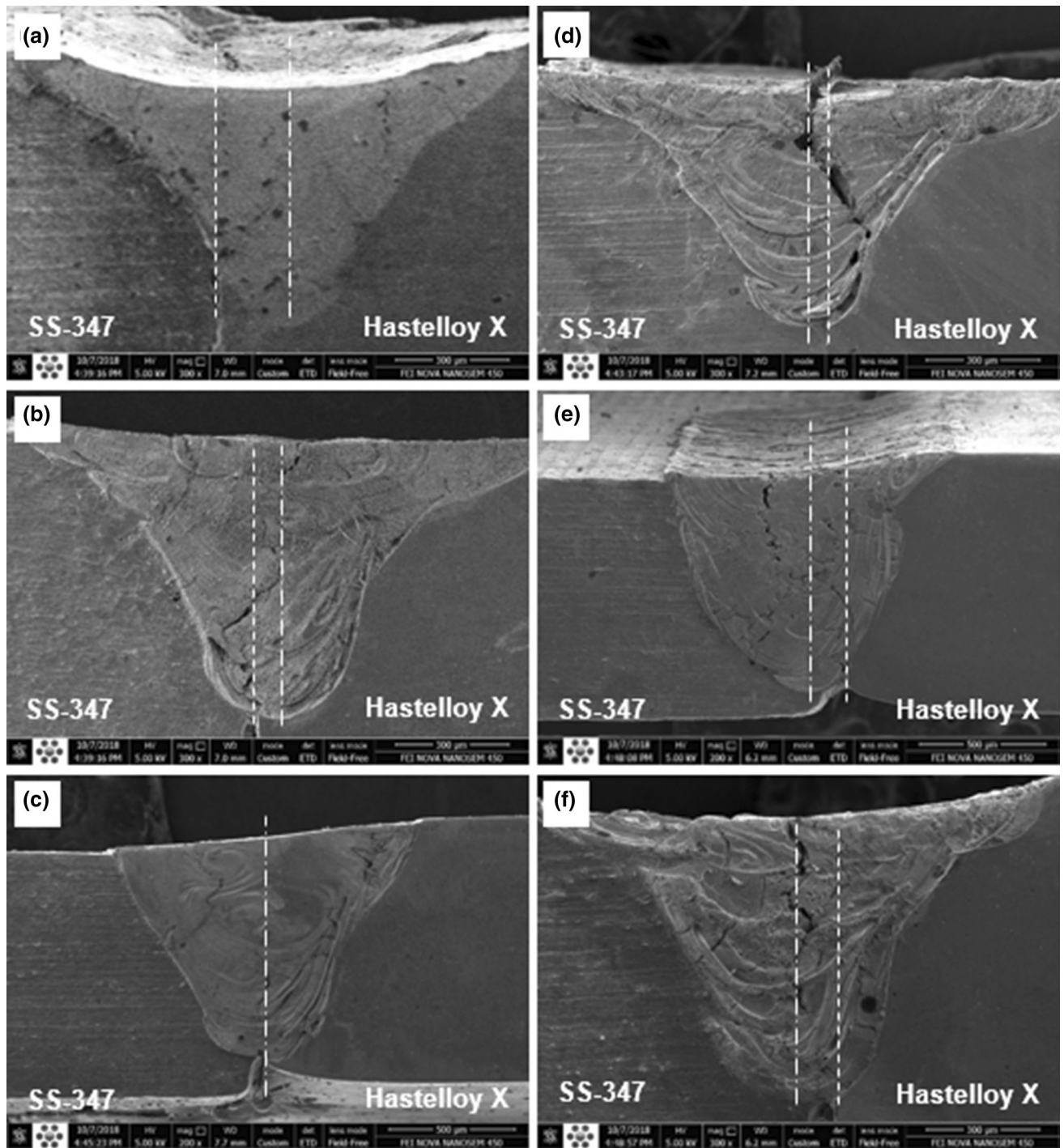


Fig. 11—Macrostructure across the weld of a Hastelloy X to 347 stainless steel with different misalignment: (a) 0.2 mm onto Hastelloy X, (b) 0.1 mm onto Hastelloy X, (c) without misalignment, (d) 0.1 mm onto 347, (e) 0.2 mm onto 347, (f) 0.3 mm onto 347.

total diffusivity of the melt at the terminal solidification state is considerably reduced, as shown in Figure 14(a), and hence hinder dendrite coalescence. Decreasing diffusivity can significantly increase the steepness of the $T-(f_s)^{1/2}$ curves at high f_s (Figure 14(b)) and increase the solidification cracking susceptibility caused by the solidification ends at lower temperatures closely

eutectic temperature. It was mentioned that the predicted $T-(f_s)^{1/2}$ curves from phase-field simulations was derived by the method of Geng *et al.*^[12] work.

As seen in Figures 15(a) and (c), a notable distinction of Fe and Ni was distinguished across 347 SS/fusion zone and fusion zone/Hastelloy X interfaces due to their high diffusion rate in the molten zone. The element

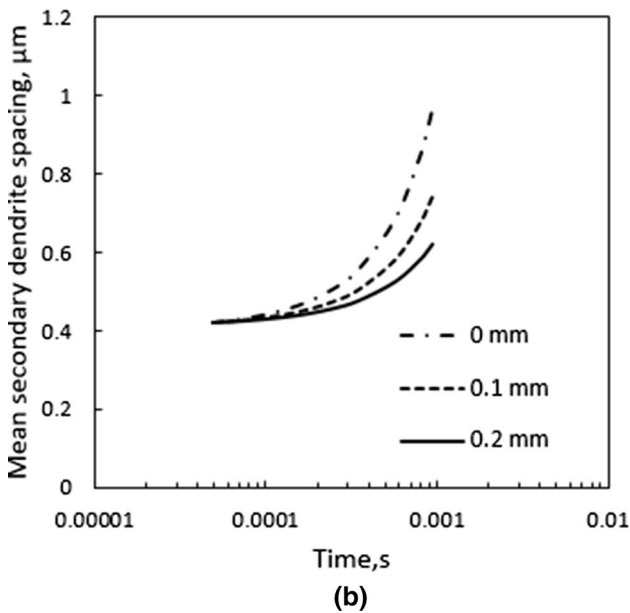
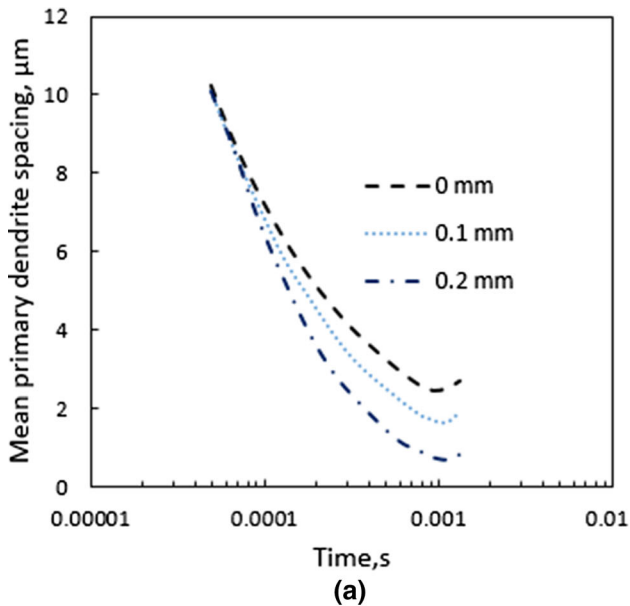


Fig. 12—(a) Average primary dendrite spacing, (b) secondary dendrite arm spacing as functions of time in laser welding for various alloy compositions according to 0, 0.1 and 0.2 mm offset to Hastelloy X.

concentration on a macroscopic proportion is almost unfluctuating in the weld pool, due to forceful swirling convective intermingling of the metal in the molten state.

As seen in Figure 16, the spreading of the elements in the weld pool is tangible when comparing the mean percentages with the areal maps. The equiaxed cellular structure is extremely contingent on the alloy composition, molten flow, and thermal gradients at the solid/liquid interface. As divulged by model and EDS, the chemical composition of the fusion zone was established upon a combination of both Hastelloy X and stainless steel 347 has a wide variety between liquidus and solidus

temperatures that were optimized for the formation of the equiaxed cellular structures. Because the undercooled domain range in the weld center is comparatively high,^[22] more equiaxed dendrites fertilize in the forefront of the columnar dendrite tips and conquer the growth path of the columnar dendrites. Accordingly, the columnar dendrites would be entirely obstructed and the CET takes place. The requirement for critical local constitutional undercooling for the growth of equiaxed dendrites has also been noted by Badillo and Beckermann.^[26] Further, at a welding speed of 3.5 mm/s, it can be found that the equiaxed dendrite takes place at a specified temperature gradient lower than 2300 K/mm where the cooling rate at the CTE interface was 1.4×10^4 K/s.

C. Effect of Fluid Flow

As known, the Marangoni convection is an occurrence of interfacial irregular fluid flow stimulated by surface tension gradients which may be provoked by concentration, temperature, and surface gradients infuse with the interface, nevertheless, it is realized that this phenomenon impressively increases the melt transmission speed through the interface. The Marangoni effect caused the fluid flow from the higher temperature locale into the lower temperature zone in the weld pool. It is worth noting that the concave joint surface in Figures 9(a) through (f) was owing to the Marangoni convection and surface tension that has been shown by numerical simulation.^[27] Given that the maximum surface velocity takes place quite adjacent to the rim of the pool surface, the convection tends to press up the pool surface near the edge so that the pool surface is elongated at the upper zone of the weld pool as seen in Figure 9.

Figure 17 illustrates solidified convection swirls from the mixed liquids of different alloys in the weld zone. Macrosegregation was observed due to the lack of weld pool mixing, as the fluid flow was upward in the vicinity of the interface of Hastelloy X and stainless steel 347 and the velocity component normal to the interface was inadequate to intermingle the two molten metals.

Moreover, the multiple orientations of dendrite growth can be distinguished in eutectic microstructure configurations in the weld melt, as demonstrated in Figure 17(b). Surface flow motion in the weld pool arises commonly from Marangoni stress. In conduction-mode laser beam welding, the surface tension of the weld metal reduces by raising the temperature, namely, $\partial\gamma/\partial T < 0$. In this case, fluid is forced into the interdendritic areas of the weld pool, bringing about a decrease of the hot cracking susceptibility.^[28]

The variation in solute concentration gives rise to an increase or decrease of Marangoni tension, thereby inducing different magnitude of fluid flow in the weld melt. Even though the fluid flow attains high velocities in laser welding, which bring about considerable mass transport, there are only just phase-field models in the conduction-mode laser welding that attempt to rationalize the influence of the weld melt flow on the

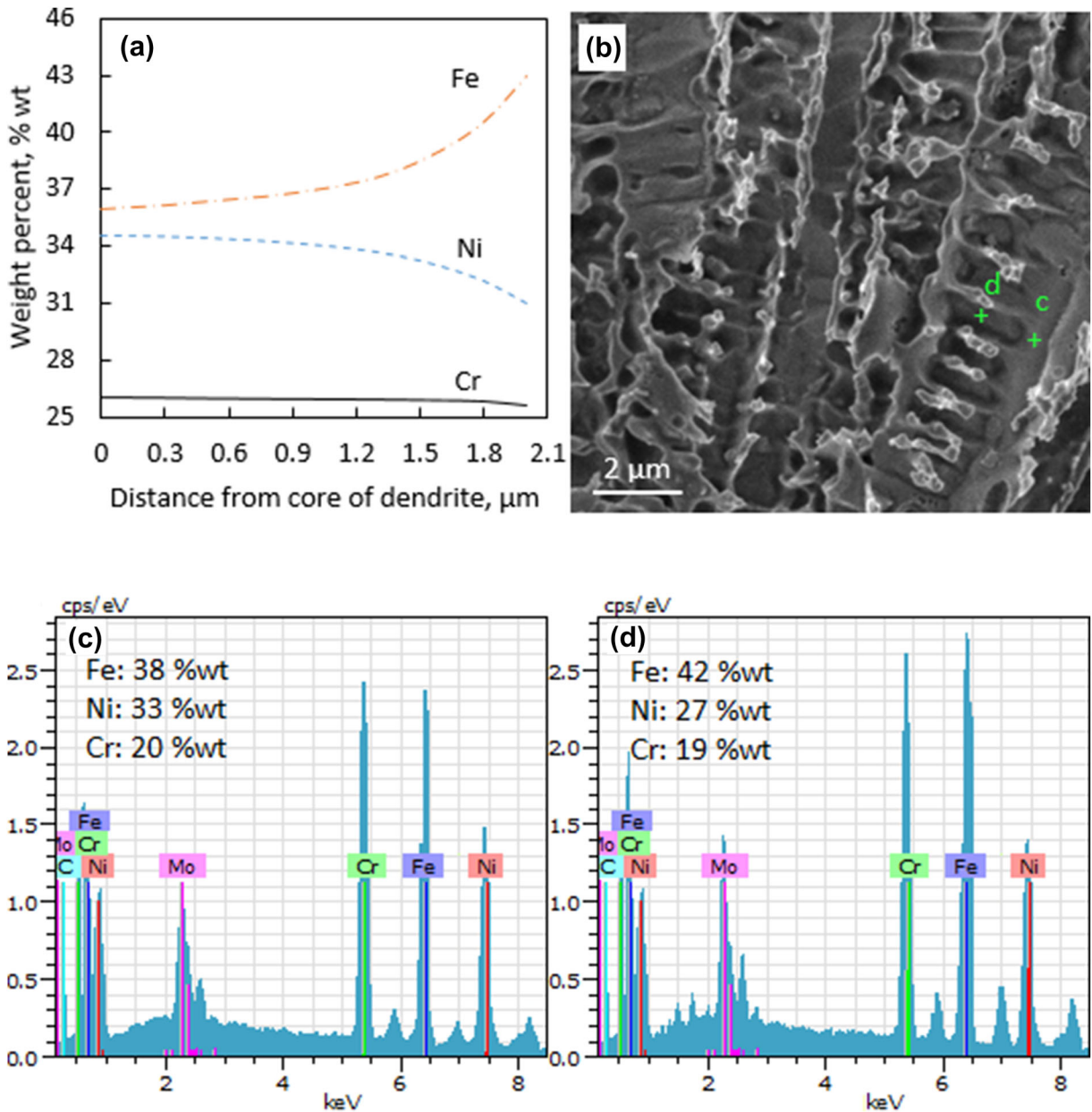


Fig. 13—(a) Predicted composition encompassed in the core of dendrites and at the interdendritic area, (b) scanning electron micrograph of columnar dendrites, (c) EDS spectrum of the point c in the core of dendrite, (d) EDS spectrum of the point d at the interdendritic area.

morphology of microstructure. To scrutinize the effect of the Marangoni effect on fluid flow, a model was fulfilled at a negative $\partial\gamma/\partial T$ which was consistent with Table III. As seen in Figure 18, the rate of fluid flow changes microstructure characteristics, in particular, mean primary and secondary dendrite arm spacing.

Melt convection can circulate dendrite fragments that are separated from the columnar dendrite colonies into the bulk liquid. Fragments of dendrite perform similar nucleation sites for equiaxed dendrites supporting the CET. Also, melt convection brings about a higher cooling rate and motivation of CET manifestation compared to the non-convecting case.^[29]

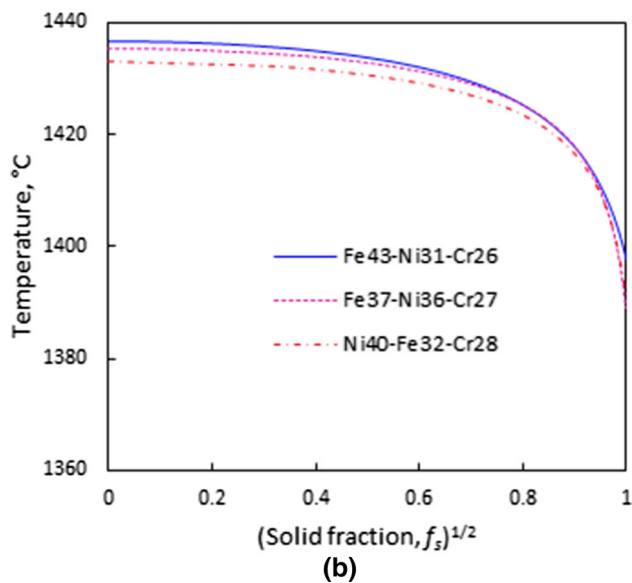
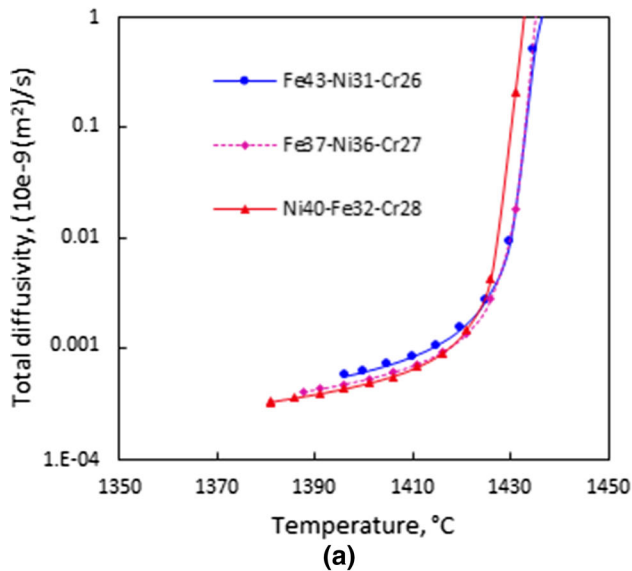


Fig. 14—(a) Predicted total diffusivity of the melt, (b) predicted $T-(f_s)^{1/2}$ curves from phase-field simulations for various alloy compositions according to 0, 0.1 and 0.2 mm offset to Hastelloy X.

D. Prediction of the Optimum Range of Welding Parameters

The steady-state tip velocity is an appropriate criterion for distinguishing phase-field results toward dendritic growth techniques. In the computational model, tip velocity is derived from the temporary evolution of $\phi = 0$ in the direction of the primary dendrite growth axis. Figure 19 showed that the higher the tip velocity, the larger the undercooling due to low time to grow, and the smaller the radius of the dendrite tip.

As can be seen in Figure 7, two types of dendrite morphology were observed that are an extremely advanced side-branch morphology and of the suppressed secondary dendrite. In the entirely melt

convection process thereupon high undercooling, the attenuated thermal diffusion film takes advantage of the liberation of latent heat and progresses to secondary dendrites evolution, consequently, the promotion of primary dendrite reveals a highly developed secondary dendrite morphology. Furthermore, under partially melt flow, the tip velocity subject to high undercooling is faster than that under low undercooling, therefore the thermal diffusion layer subject to high undercooling melt is thinner than that under the influence of low undercooling melt, which gives rise to primary dendrites encircled by a thicker thermal diffusion film. The thermal diffusion film suppresses the liberation of latent heat and demarcates the non-smooth motion of the interface accordingly, secondary dendrites are impeded.

The optimum range of welding parameters brought about by defect-free weld metal as illustrated in Figure 20.

In this area, mechanical properties of weld metal were approximately 80 pct of the mechanical properties of Hastelloy X and 87 pct of stainless steel 347, as shown in Figure 21. At a condition where the primary dendrite spacing is very low, almost lower than $1 \mu\text{m}$, backfilling phenomena will not take place during the final solidification of the weld pool, thus increasing the probability of the occurrence of solidification crack. On the other hand, provided that the primary dendrite spacing is very high, almost higher than $3 \mu\text{m}$, the segregation of Nb, Mo compound at interdendritic regions is possible and the solidification cracking susceptibility has increased.

Solidification cracking transpires when the volumetric solidification contraction results from the dissimilarity between the density of liquid and solid phases by passing the maximum volumetric flow rate per unit volume. The solidification cracking sensitivity of the welds is dependent on the weld metal dilution level. As demonstrated in Figure 20 molten zone with lower dilution is not prone to solidification cracking because there is no low melting point eutectic existing in the grain boundary to result in solidification cracking. The relatively defective cracking resistance of welds disposed at higher dilution levels is described as having a broad solidification temperature domain and growing the quantity of secondary phase which develops by increasing dilution. Since the laser beam offset inclines to 347 stainless steel, Moreover, the comparatively high cracking susceptibility is chiefly ascribed to the high amount of Si that is noticeably mentioned in Reference 30, which predisposes to segregate with Mn, Cr, and Mo as compounds by low melting point in the final solidification stage.

Substantial changes in microstructure evolution with welding parameters can be perceived for both equiaxed and columnar dendrites. It appears that a weld pool made by welding parameters window is shown in Figure 20 with a high proportion of equiaxed dendrites to columnar dendrites having a lower susceptibility to cracking. In fact, a fine equiaxed dendritic morphology by plentiful liquid between the grains can deform more simply subject to stress than a coarse columnar dendritic structure.

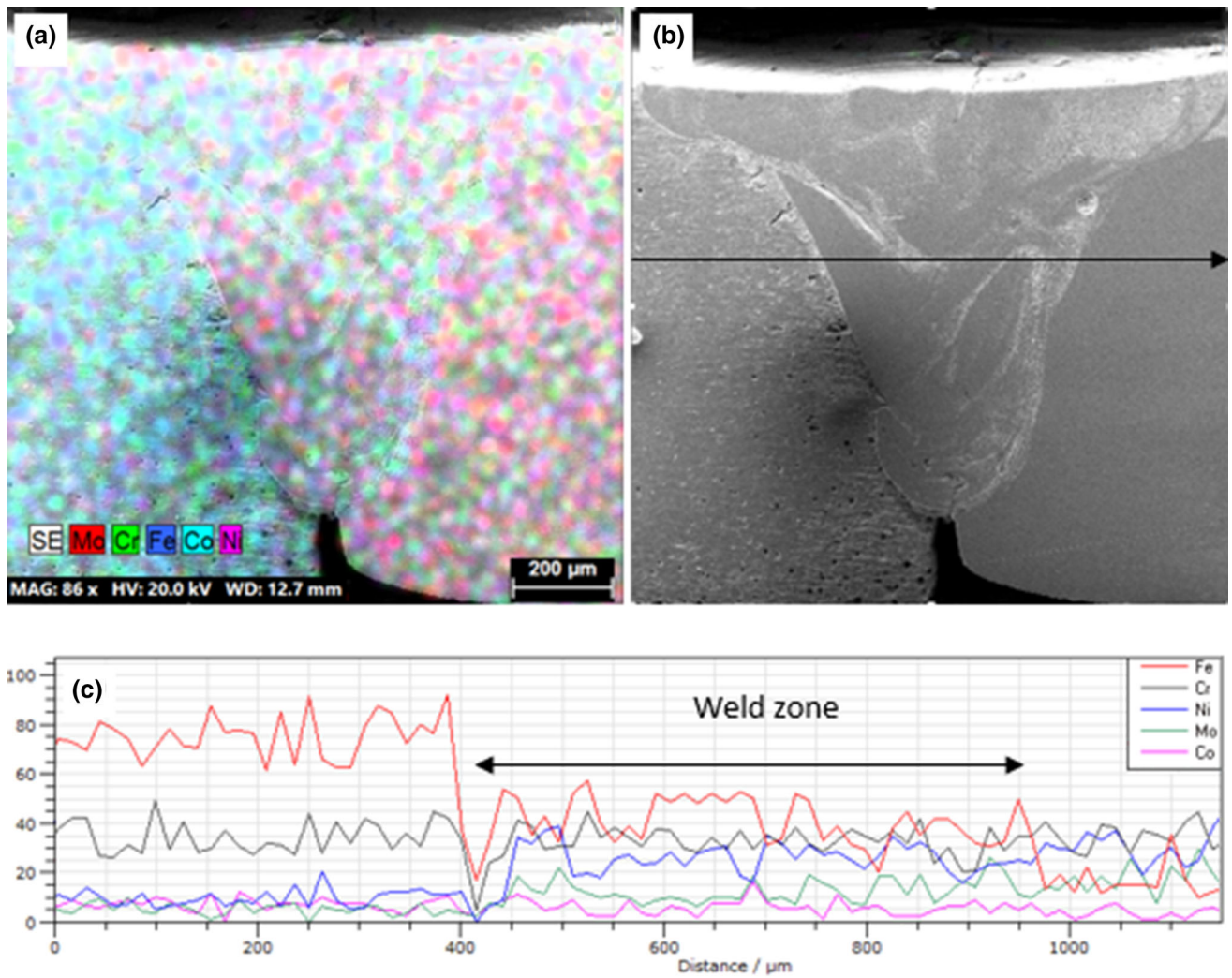


Fig. 15—(a) The EDS map spectrum of element concentration on a macroscopic proportion in the weld pool, (b) Macrostructure across the weld of a Hastelloy X to 347 stainless steel without misalignment, (c) the EDS line spectrum of the line drawn in the weld zone in the part b.

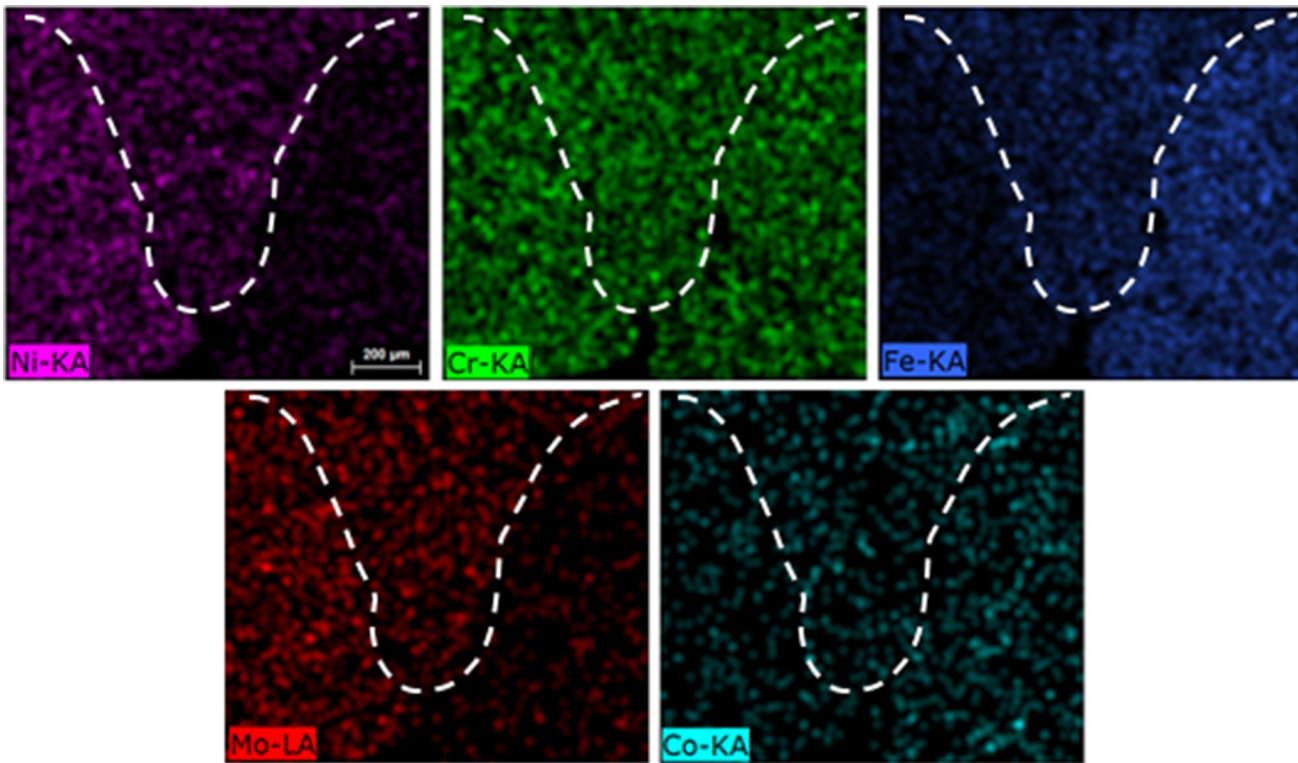


Fig. 16—Areal maps for the distribution of Ni, Fe, Cr, Mo and Co in the cross-section of the weld pool.

VI. CONCLUSIONS

A computational model is utilized to study the effects of dilution level and Marangoni convection on the morphology of the columnar and equiaxed dendrite and the effect on the primary dendrite spacing in dissimilar pulsed laser welded Hastelloy X to 347 stainless steel alloys. The following important items could be inferred from this paper:

1. The morphology of the columnar and equiaxed dendrite inside the weld metal and the alloy composition in the core of the dendrites and at the inter-

dendritic area was distinguished by experimental analysis and the phase-field model, which were well matched. Therefore, the phase-field model was utilized to relate the solidification behavior of dendrites to the microscopic properties of the weld metal.

2. The laser beam offset is more critical in microstructure evolution, which causes a finer structure and a minimum spacing between columnar dendrites for a 0.2 mm beam offset.
3. The secondary dendrite arm spacing decreases with increasing equivalent concentration of Ni and Cr by decreasing dilution.

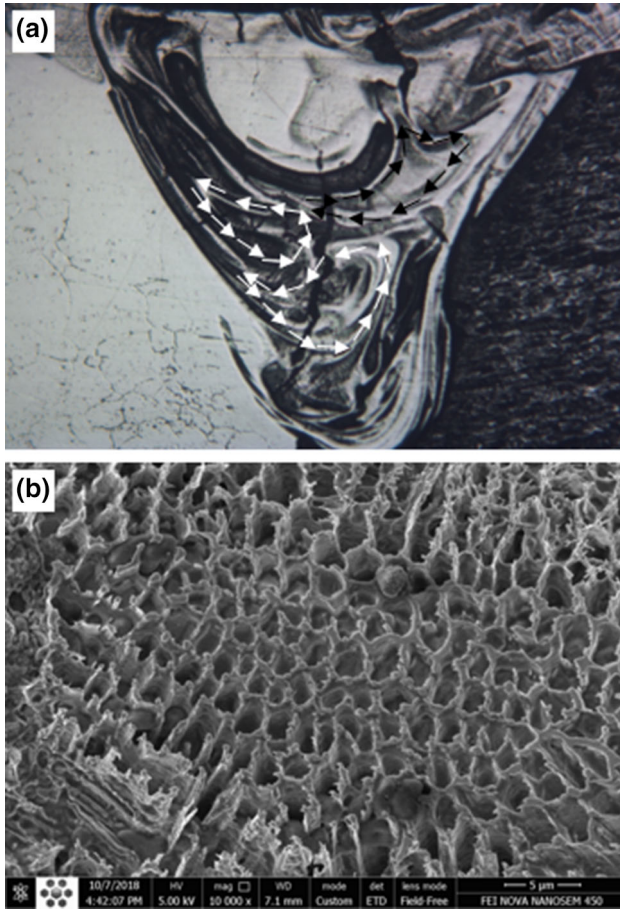


Fig. 17—Microstructure of weld pool showing (a) convection swirls, (b) orientation of dendrite growth.

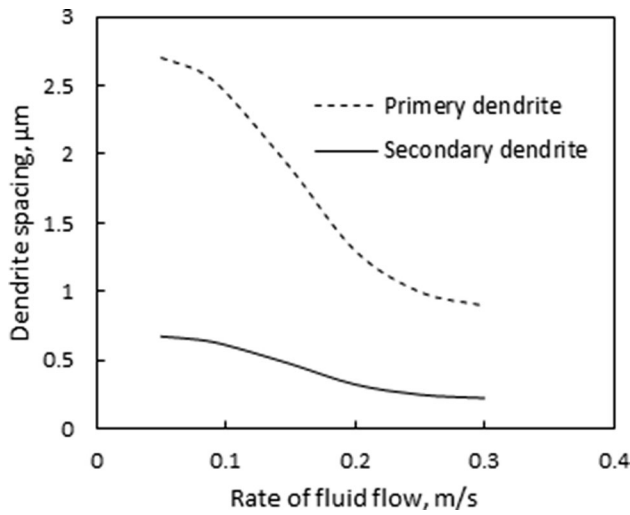


Fig. 18—Mean primary and secondary dendrite arm spacing as functions of the rate of fluid flow.

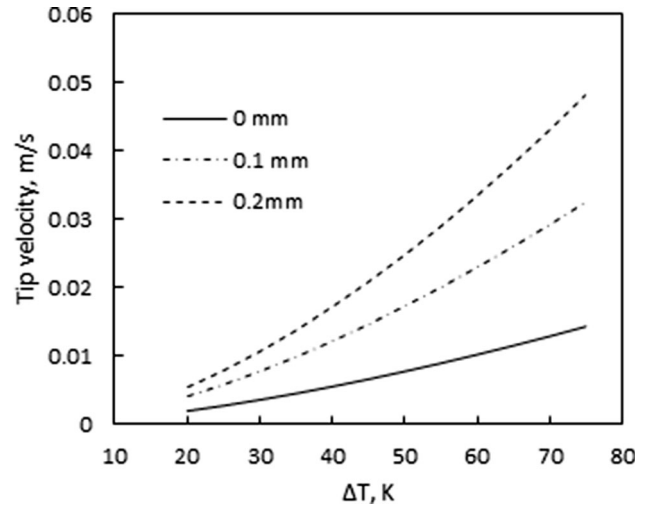


Fig. 19—Tip velocity versus undercooling simulated for various alloy compositions according to 0, 0.1 and 0.2 mm offset to Hastelloy X.

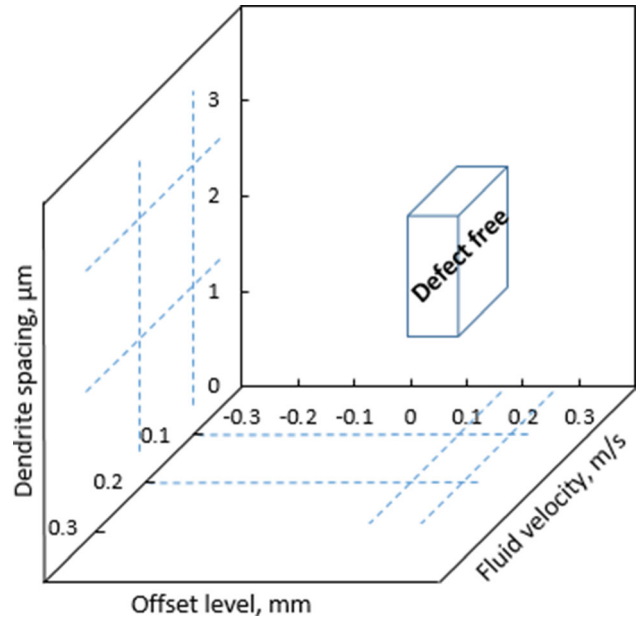


Fig. 20—The optimum range of welding parameters that cause the defect free weld metal.

4. Mechanical properties of weld metal were approximately 80 pct of the mechanical properties of Hastelloy X and 87 pct of stainless steel 347.
5. As a condition where the primary dendrite spacing is lower than 1 μm , the probability of the occurrence of solidification crack increases.
6. Provided the primary dendrite spacing is higher than 3 μm , the segregation of Nb, Mo compound in

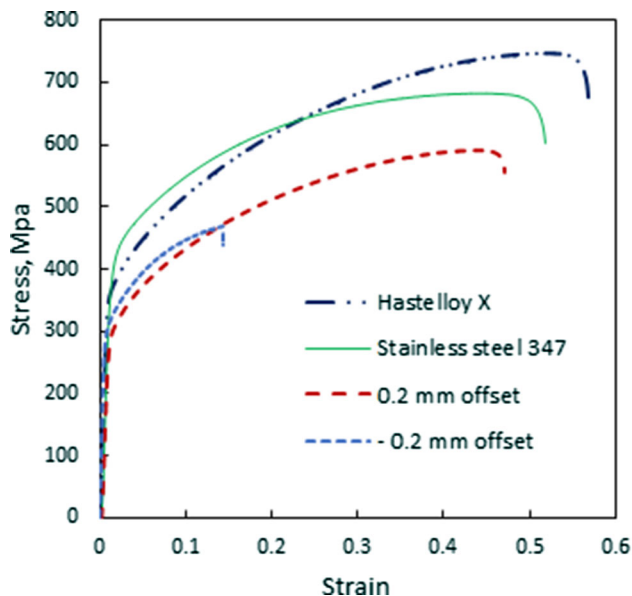


Fig. 21—The stress-strain curves of dissimilar pulsed laser welded Hastelloy X to stainless steel 347 at different offset levels.

interdendritic regions is possible and the solidification cracking susceptibility increases.

ACKNOWLEDGMENTS

The authors express their gratitude to the University of Tehran for providing facilities and equipment.

REFERENCES

1. M.R.N. Esfahani, J. Coupland, and S. Marimuthu: *J. Mater. Process. Technol.*, 2015, vol. 224, pp. 135–42.
2. K. Hao, M. Gao, R. Wu, and X. Zeng: *J. Mater. Process. Technol.*, 2020, vol. 275, art. no. 116330.
3. W. Kurz, C. Bezençon, and M. Gäumann: *Sci. Technol. Adv. Mater.*, 2001, vol. 2, pp. 185–91.
4. X.H. Zhan, Z.B. Dong, Y.H. Wei, and R. Ma: *J. Cryst. Growth*, 2009, vol. 311, pp. 4778–83.

5. A. Farzadi, M. Do-Quang, S. Serajzadeh, A.H. Kokabi, and G. Amberg: *Model. Simul. Mater. Sci. Eng.*, 2008, vol. 16, art. no. 065005.
6. D. Montiel, L. Liu, L. Xiao, Y. Zhou, and N. Provatas: *Acta Mater.*, 2012, vol. 60, pp. 5925–32.
7. V. Fallah, M. Amoozrezaei, N. Provatas, S.F. Corbin, and A. Khajepour: *Acta Mater.*, 2012, vol. 60, pp. 1633–46.
8. W.J. Zheng, Z.B. Dong, Y.H. Wei, K.J. Song, J.L. Guo, and Y. Wang: *Comput. Mater. Sci.*, 2014, vol. 82, pp. 525–30.
9. N.S. Bailey, K.-M. Hong, and Y.C. Shin: *Comput. Mater. Sci.*, 2020, vol. 172, art. no. 109291.
10. F. Yu, Y. Wei, Y. Ji, and L.-Q. Chen: *J. Mater. Process. Technol.*, 2018, vol. 255, pp. 285–93.
11. M. Gaoyang, X. Lingda, W. Chunming, J. Ping, and Z. Guoli: *Mater. Des.*, 2019, vol. 181, art. no. 107980.
12. S. Geng, P. Jiang, X. Shao, G. Mi, H. Wu, Y. Ai, C. Wang, C. Han, R. Chen, and W. Liu: *Scr. Mater.*, 2018, vol. 150, pp. 120–24.
13. P. Nie, O.A. Ojo, and Z. Li: *Acta Mater.*, 2014, vol. 77, pp. 85–95.
14. J.A. Dantzig and L.S. Chao: in *10th U.S. Natl. Cong. Appl. Mech.*, J.P. Lamb, ed., ASME, 1986, pp. 249–55.
15. J.-H. Jeong, N. Goldenfeld, and J.A. Dantzig: *Phys. Rev. E*, 2001, vol. 64, art. no. 041602.
16. A. Zhang, S. Meng, Z. Guo, J. Du, Q. Wang, and S. Xiong: *Metall. Mater. Trans. B*, 2019, vol. 50B, pp. 1514–26. <https://doi.org/10.1007/s11663-019-01549-5>.
17. Y. Zhao, B. Zhang, H. Hou, W. Chen, and M. Wang: *J. Mater. Sci. Technol.*, 2019, vol. 35, pp. 1044–52.
18. T. Suzuki, M. Ode, S.G. Kim, and W.T. Kim: *J. Cryst. Growth*, 2002, vols. 237–239, pp. 125–31.
19. H. Kobayashi, M. Ode, S.G. Kim, W.T. Kim, and T. Suzuki: *Scr. Mater.*, 2003, vol. 48, pp. 689–94.
20. S.G. Kim: *Acta Mater.*, 2007, vol. 55, pp. 4391–99.
21. J. Kundin, L. Mushongera, and H. Emmerich: *Acta Mater.*, 2015, vol. 95, pp. 343–56.
22. T. Azimzadegan and S.A.A.A. Mousavi: *J. Manuf. Process.*, 2019, vol. 44, pp. 226–40. <https://doi.org/10.1016/j.jmappro.2019.06.005>.
23. R. Siquieri, J. Rezende, J. Kundin, and H. Emmerich: *Eur. Phys. J. Spec. Top.*, 2009, vol. 177, pp. 193–205.
24. L. Wang, Y. Wei, F. Yu, Q. Zhang, and Q. Peng: *Cryst. Res. Technol.*, 2016, vol. 51, pp. 602–09.
25. J.N. Dupont, S.W. Banovic, and A.R. Marder: *Weld. J.*, 2002, vol. 7, pp. 374–83.
26. A. Badillo and C. Beckermann: *Acta Mater.*, 2006, vol. 54, pp. 2015–26.
27. M.C. Tsai and S. Kou: *Int. J. Numer. Methods Fluids*, 1989, vol. 9, pp. 1503–16. <https://doi.org/10.1002/flid.1650091206>.
28. D.L. Olson and G.R. Edwards: *Philos. Trans. R. Soc. A*, 1998, vol. 356, pp. 927–40. <https://doi.org/10.1098/rsta.1998.0197>.
29. A. Kumar and P. Dutta: *J. Mater. Sci.*, 2009, vol. 44, pp. 3952–61.
30. S. Chen, X.-X. Ye, D.K.L. Tsang, L. Jiang, K. Yu, C. Li, and Z. Li: *J. Mater. Sci. Technol.*, 2019, vol. 35, pp. 29–35.

Publisher's Note Springer Nature remains neutral with regard to jurisdictional claims in published maps and institutional affiliations.